Proceedings of the Thirty-sixth (2026) International Ocean and Polar Engineering Conference **www.isope.org**
Orlando, Florida, USA, May 31-June 5, 2026

ISBN 978-1-880653-72-2; ISSN 1098-6189

Effect of Different Gas Layer Baffles on Gas Content at the Propeller Disk in Gas Layer Drag Reduction

Zhiqiang Liu[a], Xiaosong Zhang[a], Shan Wang[a], Jingpu Chen[a], Decheng Wan[b,]*

[a] Shanghai Branch, China Ship Scientific Research Center, Shanghai, China
[b] Computational Marine Hydrodynamic Lab (CMHL), School of Ocean and Civil Engineering,
Shanghai Jiao Tong University, Shanghai, China
*Corresponding author

ABSTRACT

Air layer drag reduction (ALDR) is an important aspect of green ship development and also an important component in the numerical study on ship hydrodynamics. In this study, a full-scale ship is taken as the research object, with multiple rows of gas injection holes and baffles installed on the ship's bottom. By opening holes in the gas baffles at the stern of the hull, the effect of different hole-opening cases on the gas content of the stern propeller disk is investigated. Numerical calculations are conducted using the two-phase flow solver of the OpenFOAM platform, and the Volume of Fluid (VOF) method is employed for gas-liquid two-phase flow interface capturing. To study the evolution of the air layer at the ship bottom under full-scale conditions, a full-scale model is adopted for calculations, focusing on investigating the changes of the hull air layer and its influence on the gas content of the stern propeller disk plane. This work aims to guide the design and development of engineering and lay a foundation for subsequent studies on the influence of the air layer on the hydrodynamic performance of propellers.

KEY WORDS: air layer drag reduction, OpenFOAM, VOF, gas baffles opening-hole, gas content.

INTRODUCTION

The development of green ship technology has been one of the important components in the maritime industry. Hull form optimization, energy-saving devices, wind-assisted propulsion technology, and others can effectively reduce ship resistance performance, thereby lowering carbon dioxide emissions. Air Layer Drag Reduction (ALDR) technology is also a vital technical aspect in the development of green ships: air injection mechanisms are installed at the ship hull bottom to form an air layer, which reduces the hull's frictional drag and further decreases overall ship resistance, show as
Fig. 1. In terms of experimental and numerical studies on ALDR, scholars have conducted in-depth research.
Mäkiharju et al. (2012) explored the applicability of air lubrication technology to large ocean-going ships and the U.S. Great Lakes ships by utilizing data from the literature, establishing basic energy-economic calculations, and presenting energy-saving results for a hypothetical air-lubricated ship. The analysis indicates that if successfully implemented, both air layer drag reduction and partial cavitation drag reduction could yield an energy savings of 10% to 20%, along with a corresponding reduction in emissions. Elbing et al. (2013) conducted an investigation on air-induced drag reduction of a 12.9 m-long flat plate test model under the condition of a free stream speed of 6.3 m/s, with the maximum Reynolds number exceeding 80 million. At a downstream distance of up to 11.5 m, qualitative and quantitative flow field information was acquired, including local skin friction, void fraction profiles, and gas-liquid velocity profiles. A scaling of the air flux for ALDR was developed from balancing shear-induced lift forces and buoyancy forces on a single bubble within a shear flow. The results showed that the air layer thickness was nominally three-quarters of the total volumetric flux (per unit span) of air injected divided by the free stream speed. Jagdish et al. (2014) captured and retained the air layer by means of hydrophobic plates to enhance the feasibility of the microbubble drag reduction technology. Physical experiments demonstrate that a moving flat plate can carry an air layer around it, thereby reducing friction. This work has laid a research foundation for subsequent studies on air layer drag reduction of ships.

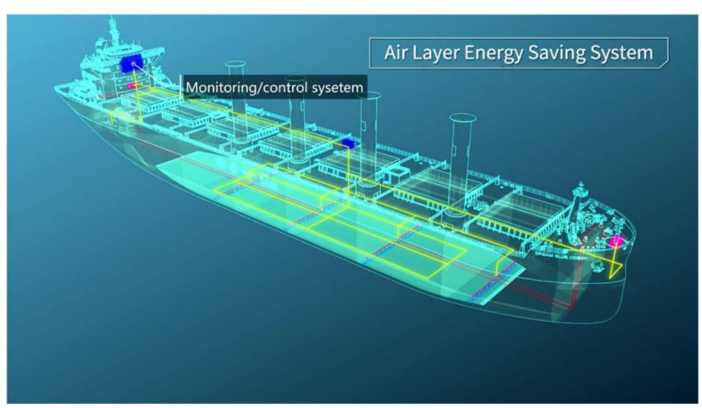

Fig. 1Air Layer Drag Reduction schematic diagram (ALDR)

Yanuar et al. (2018) obtained the optimal type of air lubrication via microbubble drag reduction and air layer drag reduction technologies to reduce the drag of a 56 m-long Indonesian Self-Propelled Barge (SPB), and conducted towing tests on the ship model. The sailing speed varied within a Froude number range of 0.11–0.31. The air injection rate was set at 80, 85, and 90 L/min, while the microbubble injection coefficient ranged from 0.20 to 0.60. The results indicate that the ship model equipped with the air layer achieved the highest drag reduction rate, up to 90%. Hao et al. (2019) conducted an experimental study on drag reduction by an air layer under a flat plate in a towing tank. The shape of the air layer was observed, and the change in drag was measured. The results show that under specific air injection conditions, the drag reduction method using an air layer in the bottom cavity can effectively reduce frictional drag. Simultaneously, resistance and self-propulsion tests were carried out on a model ship based on a 95,000 DWT bulk carrier in the towing tank. The bottom air layer was observed, and the expected power saving was estimated. The results indicate that the power output of the full-scale ship can be reduced by 15%. Wu and Ou (2019) conducted model test studies on the ALDR method with different bottom cavity depths. During the tests, the evolution of the air layer was observed, and the changes in drag were measured. The results of the model tests showed that the total drag reduction rate was approximately 20% at the ship's designed sailing speed. In wave environments, the air layer was prone to breakage, which reduced the drag reduction rate in short waves; in long waves, it still exhibited a favorable drag reduction effect. Zhang et al. (2020) performed a numerical study on the ship drag reduction rate with the Wing Air Injection Pipe (WAIP) device based on the open-source toolbox OpenFOAM, aiming to improve the efficiency of the propulsion system. Numerical results indicate that the drag reduction rate is closely related to the submersion depth of the hydrofoil, the angle of attack of the hydrofoil, and the pressure at the air inlet, and is proportional to the air flow rate. An et al. (2022) reviewed the research progress of air lubrication drag reduction technology from both experimental and numerical aspects, which is mainly categorized into three drag reduction methods: microbubble drag reduction (injecting microbubbles along the ship hull), air layer drag reduction (covering the ship bottom with a large air layer), and air cavity drag reduction (filling the recesses under the ship hull with air). The paper elaborates on the typical experimental phenomena of the three drag reduction methods and the theoretical achievements of numerical studies, revealing the essence that air lubrication technology achieves drag reduction by altering the physical properties of the turbulent boundary layer. Zhao and Zong (2022) conducted experimental and numerical studies on AIDR (Air-Injection Drag Reduction) of a ship model. During the experiments, the AIDR effect of the ship model was investigated under one draft and three sailing speeds. Subsequently, two numerical models—namely the Euler-Euler two-fluid model and the Volume of Fluid (VOF) model—were employed to simulate the AIDR effect. The results indicate that at low air flow rates, Microbubble Drag Reduction (MBDR) plays a dominant role; at high air flow rates, air layer drag reduction dominates; and a transition region exists at moderate air flow rates. Ships with higher sailing speeds are more conducive to achieving AIDR. Mohamad et al. (2025) conducted experimental studies using a flat plate in a towing tank, investigating the drag reduction effect of the technology under different Froude numbers. The results indicate that air lubrication efficiency is relatively dependent on the flow Reynolds number and boundary layer thickness. It was found that turbulent effects facilitate the coexistence of the air layer and the transitional boundary layer. However, air lubrication in the laminar flow regime may lead to a limited increase in total drag.

In this paper, taking a full-scale ship as the research object, macro-scale research on air layer drag reduction (ALDR) is conducted by installing an air layer device at the ship hull bottom. By setting different opening-hole sizes for the air layer baffle at the ship stern, the influence of the baffle openings on the gas content at the stern propeller disk plane is investigated. Section 2 presents the introduction to numerical theories. Section 3 focuses on air layer simulation calculations, mainly including the design of the air layer baffle opening hole, the setting of numerical simulation parameters, and the analysis of simulation results. Section 4 provides a comprehensive summary of the entire paper.

METHODS

Governing Equations

In this paper, we adopt a three-dimensional unsteady RANS (Reynolds-Averaged Navier-Stokes) Solver. The mass conservation equation and momentum conservation equation are given as follows, respectively:

$$\frac{\partial \rho}{\partial t} + \frac{\partial}{\partial x_i}(\rho u_i) = 0 \tag{1}$$

$$\frac{\partial(\rho u_i)}{\partial t} + \frac{\partial(\rho u_i u_j)}{\partial x_j} = \frac{\partial}{\partial x_j}\left(\sigma_{ij} - \rho\overline{u_i' u_j'}\right) \tag{2}$$

In the formula, where $u_i$denotes the velocity of the mesh element, u_i' denotes the fluctuating velocity, p denotes the pressure, and σ_{ij} denotes the stress tensor.

$$\sigma_{ij} = \left(-p\delta_{ij} + \mu\left(\frac{\partial u_i}{\partial x_j} + \frac{\partial u_j}{\partial x_i}\right)\right) \tag{3}$$

Based on the Boussinesq eddy viscosity model, the Reynolds stress term is given by

$$-\rho\overline{u'_i u'_j} = \mu_t\left(\frac{\partial u_j}{\partial x_i} + \frac{\partial u_i}{\partial x_j}\right) - \frac{2}{3}\left(\rho k + \mu_t \frac{\partial u_k}{\partial x_k}\right)\delta_{ij} \tag{4}$$

Where μ_t denotes the eddy viscosity coefficient.

By adopting the VOF method, the shape of the free surface is captured via the volume fraction α_n. The volume fractions of the water phase α_{water} and the gas phase α_{air} satisfy the following equations, respectively:

$$\alpha_{water} + \alpha_{air} = 1 \tag{5}$$

In governing equations (6) and (7), the density and viscosity are taken as the weighted average of the volume fractions.

$$\rho = \alpha_{water}\rho_w + \alpha_{air}\rho_a \tag{6}$$

$$\mu = \alpha_{water}\mu_w + \alpha_{air}\mu_a \tag{7}$$

The governing equation for the volume fraction is given as follows:

$$\frac{\partial}{\partial t}\int_V \alpha_n \, dV + \int_A \alpha_n v_i \cdot da_i = -\int_A \alpha_n v_{d,i} \cdot da_i \tag{8}$$

Turbulence Model

According to the shear stress transport (SST) model:

$$\mu_t = \rho k T \tag{9}$$

Where ρ denotes the fluid density, k denotes the turbulent kinetic energy, and T denotes the turbulent time scale, the corresponding relation is given as follows:

$$T = min\left(\frac{1}{max(\omega/\alpha^*, (SF_2)/a_1)}, \frac{C_T}{\sqrt{3}S}\right) \tag{10}$$

For the mixing function F_2, the following expression holds:

$$F_2 = tanh\left(\left(max\left(\frac{2\sqrt{k}}{\beta^*\omega d}, \frac{500v}{d^2\omega}\right)\right)^2\right) \tag{11}$$

The turbulent kinetic energy (k) equation and turbulent dissipation rate (ε) equation are given as follows:

$$\frac{\partial(\rho k)}{\partial t}+\frac{\partial(\rho k u_i)}{\partial x_i}=\frac{\partial}{\partial x_i}\left[(\mu+\frac{\mu_T}{\sigma_k})\frac{\partial k}{\partial x_i}\right] - \overline{u_i^{''}u_j^{''}}\frac{\partial u_i}{\partial x_i}-\rho\beta^* k\omega \tag{12}$$

$$\frac{\partial(\rho\omega)}{\partial t}+\frac{\partial(\rho\omega u_i)}{\partial x_i} = \frac{\partial}{\partial x_i}\left[(\mu+\frac{\mu_T}{\sigma_\omega})\frac{\partial \omega}{\partial x_i}\right] - \frac{\gamma}{\mu_T}\overline{u_i^{''}u_j^{''}}\frac{\partial u_i}{\partial x_j}-\rho\beta\omega^2 + 2\rho\sigma_{\omega 2}\frac{1-F_1}{\omega}\frac{\partial k}{\partial x_j}\frac{\partial \omega}{\partial x_j} \tag{13}$$

In the formula:

$$\begin{cases} P_k = G_k + G_{nl} + G_b \\ P_\omega = G_\omega + D_\omega \end{cases} \tag{14}$$

Herein, G_k, G_b, G_{nl}, G_w, and D_w respectively describe the contributions of turbulence, buoyancy, the nonlinear term, specific dissipation generation, and the cross-diffusion term, which are given as follows, respectively:

$$G_k = \mu_t S^2 - \frac{2}{3}\rho k \nabla\cdot\boldsymbol{u} - \frac{2}{3}\mu_t(\nabla\cdot\boldsymbol{u})^2 \tag{15}$$

$$G_b = \beta\frac{\mu_t}{Pr_t}(\nabla\overline{T},\cdot\boldsymbol{g}) \tag{16}$$

$$G_{nl} = \nabla\cdot\boldsymbol{u}:(\boldsymbol{T}_{t,NL}) \tag{17}$$

$$G_\omega = \rho\gamma\left[\left(S^2-\frac{2}{3}(\nabla\cdot\bar{\boldsymbol{v}})^2\right)-\frac{2}{3}\omega\nabla\cdot\bar{\boldsymbol{v}}\right] \tag{18}$$

$$D_\omega = 2\rho(1-F_1)\sigma_{\omega_2}\frac{1}{\omega}\nabla k\cdot\nabla\omega \tag{19}$$

In these formulas, the factors are defined as follows:

$$\sigma_k = F_1\sigma_{k_1} + (1-F_1)\sigma_{k_2} \tag{20}$$

$$\beta^* = F_1\beta_1^* + (1-F_1)\beta_2^* \tag{21}$$

$$\sigma_\omega = F_1\sigma_{\omega_1} + (1-F_1)\sigma_{\omega_2} \tag{22}$$

$$\beta = F_1\beta_1 + (1-F_1)\beta_2 \tag{23}$$

$$\gamma = F_1\gamma_1 + (1-F_1)\gamma_2 \tag{24}$$

Where $\sigma_{k_1} = 0.85$, $\sigma_{k_2} = 1$. $\beta_1^* = 0.9$, $\beta_2^* = 0.9$. $\sigma_{\omega_1} = 0.5$, $\sigma_{\omega_2} = 0.856$. $\beta_1 = 0.075$, $\beta_2 = 0.0828$. $\gamma_1 = \frac{\beta_1}{\beta^*} - \frac{\sigma_{\omega_1}\kappa^2}{\sqrt{\beta^*}}$, $\gamma_2 = \frac{\beta_2}{\beta^*} - \frac{\sigma_{\omega_2}\kappa^2}{\sqrt{\beta^*}}$, $\kappa = 0.41$

F_1 is a function that describes the mixing application of the k-ω (k-omega) model and the k-ε (k-epsilon) model, which is given as follows:

$$F_1 = tanh\left(\left[min\left(max\left(\frac{\sqrt{k}}{0.09\omega d},\frac{500v}{d^2CD_{k\omega}}\right),\frac{2k}{d^2CD_{k\omega}}\right)\right]^4\right) \tag{25}$$

Where d denotes the distance to the wall, and v denotes the kinematic viscosity coefficient.

$$CD_{k\omega} = max\left(\frac{1}{\omega}\nabla k\cdot\nabla\omega, 10^{-20}\right) \tag{26}$$

SIMULATION

In this section, we conduct the air layer drag reduction simulation base OpenFOAM, the hull principal dimensions are showed in Table 1 The hull principal dimensions. The hull model is shown in Fig. 2.

Table 1 The hull principal dimensions

items	Symbol and unit	value
Length overall	Loa/m	55.4
Beam	B/m	10.0
Depth	D/m	5.67
Draft	T/m	3.5
Wetted surface area	S/m^2	790.81

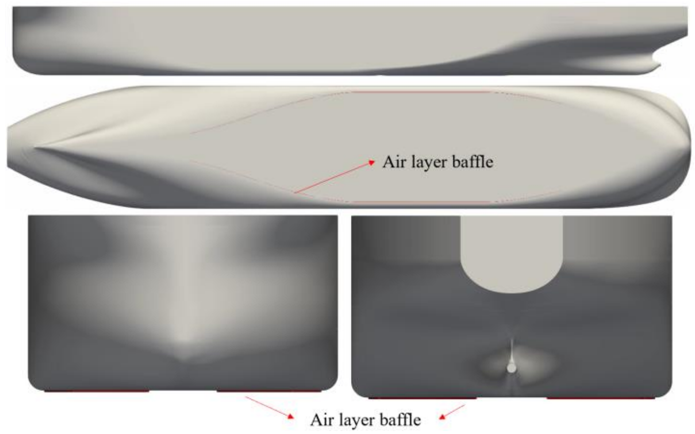

Fig. 2 hull model

Hole-Opening Cases for Ship Bottom Gas Baffles

Two air injection modules are installed at the bottom of the hull, a transverse baffle is provided at the tail end of the hull, and baffle openings of different sizes are made in the wake region. First, based on engineering practice, different baffle opening-hole forms are defined, various baffle opening methods, and the opening scheme for the tail transverse baffle are designed. The layout of the hull openings is shown in Fig. 3. The schematic diagrams of different baffle opening-holes are shown in Fig. 4.

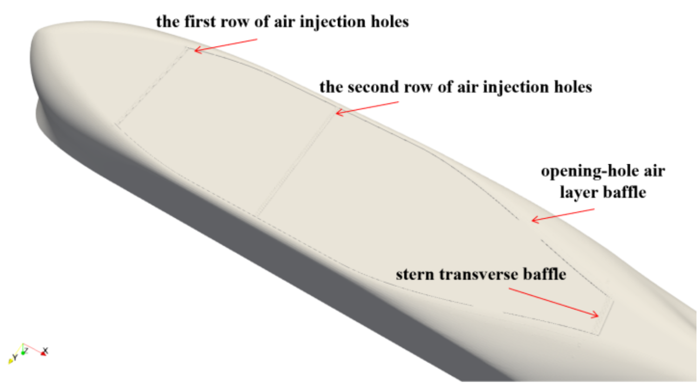

Fig. 3 Schematic diagram of the gas layer baffle at the hull bottom

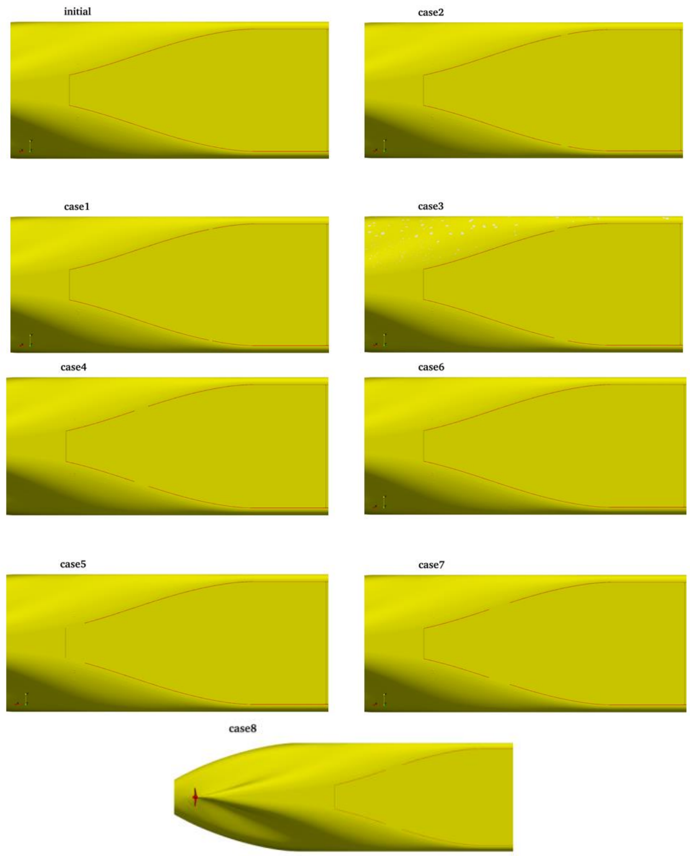

Fig. 4 Different tail opening schemes for the hull bottom gas layer baffle

Table 2 Parameters of different opening-hole schemes for hull bottom Baffles

Case	Distance from stern baffle (mm)	Length (mm)	Note
initial			
case1	10279	250	
case2	10279	500	
case3	10279	1000	
case4	5000	1000	
case5	436	1000	
case6			backopen
case7	5000	1000	case4+backopen
case8	5000	1000	case4+backopen+propeller

Table 2 presents the opening-hole parameters of different hull bottom baffles. Specifically, cases 1–5 correspond to opening-holes arranged at different positions in the stern region of the baffle, with variations in opening length dimensions. Case 6 involves openings on the baffle itself as well as on the stern transverse baffle (where "backopen" denotes that the stern transverse baffle is provided with an opening-hole), shown as Fig. 5. Case 7 adopts the same opening-hole configuration as Case 4, supplemented by openings on the stern transverse baffle. Case 8 employs the identical opening layout of Case 4 with the addition of openings on the stern transverse baffle (designed to reduce the gas content in the propeller inflow), together with the rotation operation of a propeller, to account for the impact of the propeller's rotational effect on the gas layer at the propeller disk.

The schematic diagram of the opening structure of the stern transverse baffle is illustrated in Fig. 5. The openings on the stern transverse baffle enable the trajectory diversion of the gas layer, thereby reducing the volume of gas flowing toward the propeller disk.

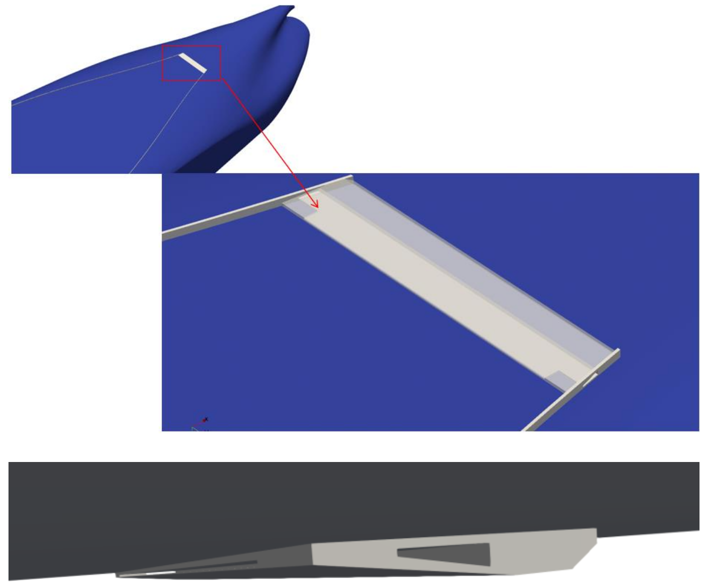

Fig. 5 Opening-hole on the stern transverse gas layer baffle

Simulation Condition Setting

Numerical simulations of different air layer baffle opening-hole configurations for the ship were carried out using OpenFOAM, with the Multiple Reference Frame (MRF) method adopted for the propeller module. Full-scale modeling was employed for the simulations. For cases without considering the propeller, half-domain calculation was implemented; whereas for cases involving the propeller, full-domain calculation was adopted.

The range of the half-domain computational domain is defined as follows: $-111\,m \le x \le 33\,m; 0\,m \le y \le 166.5m; -55.5\,m \le z \le 27.75\,m$. Two rows of air injection holes were arranged in total, with 44 air injection holes in the first row and 54 air injection holes in the second row, and the air injection velocity of the holes was set at 4.29m/s. The total mesh quantity of the half-domain reached 17.78 million. Adaptive variable step-size calculation was applied, with the maximum Courant number controlled under 1.

The meshes of the computational domain are presented in Fig. 6, Fig. 7, Fig. 8 and Fig. 9. As can be seen from the figures, given that the height of the bottom baffle is only 10mm while the overall length of the ship amounts to 55m, high-level mesh refinement is required at the ship bottom to capture fine structures such as baffles and air injection holes accurately. Consequently, the final mesh quantity is considerably higher than that required for the conventional two-phase flow resistance calculation of a ship.

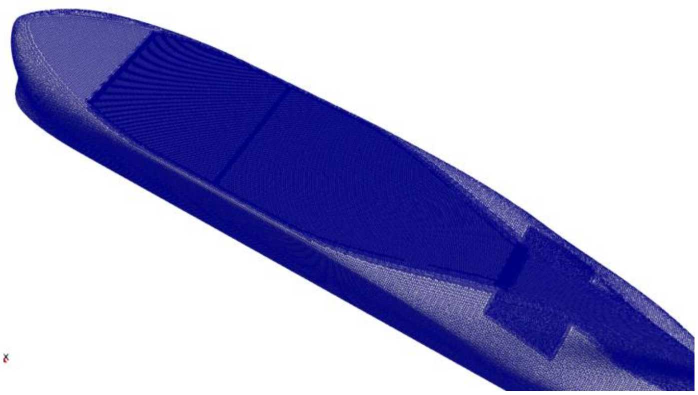

Fig. 6 The hull surface mesh

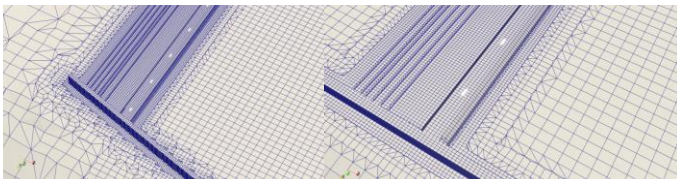

Fig. 7 Mesh at the first and second rows of air injection modules

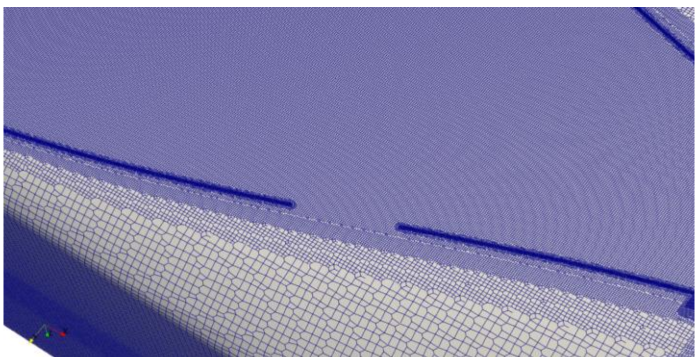

Fig. 8 Mesh at the opening of the air layer baffle

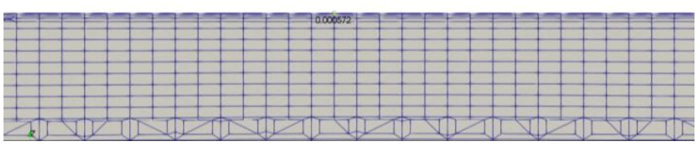

Fig. 9 boundary layer mesh of hull bottom

Analysis and Presentation of Numerical Calculation Results

Numerical calculations were performed using the two-phase flow solver interFoam based on OpenFOAM, with flow field data at different times obtained eventually. Fig. 10 depicts the instantaneous distribution of the gas layer around the hull at 120 s. As can be seen from the figure, the opening-holes on the bottom baffle of the hull can indeed function to guide the outward leakage of the gas layer and avoid the gas layer flow toward the propeller disk. This is evident in cases such as Case 4 and Case 7, where the escaping gas layer at the opening holes is clearly observable. For the schemes with opening-holes on the stern transverse baffle (e.g., Case 6), the fluid phenomenon in which the gas layer escapes toward both sides of the hull through the opening-holes can also be observed.

Compared with the cases without the propeller, the gas layer distribution at the hull stern in the cases with the propeller is significantly less extensive (as illustrated by the comparison between Case 7 and Case 8).

The principle of air-layer drag reduction technology is to form an air layer at the bottom of the hull to reduce the friction between the hull and water, thereby diminishing the frictional drag on the hull. By supplying an appropriate air injection rate at the hull bottom, the air layer can be maintained in a relatively stable form rather than being trapped within the boundary layer. Since such a stable configuration is difficult to preserve, numerical simulation is employed to investigate this phenomenon.

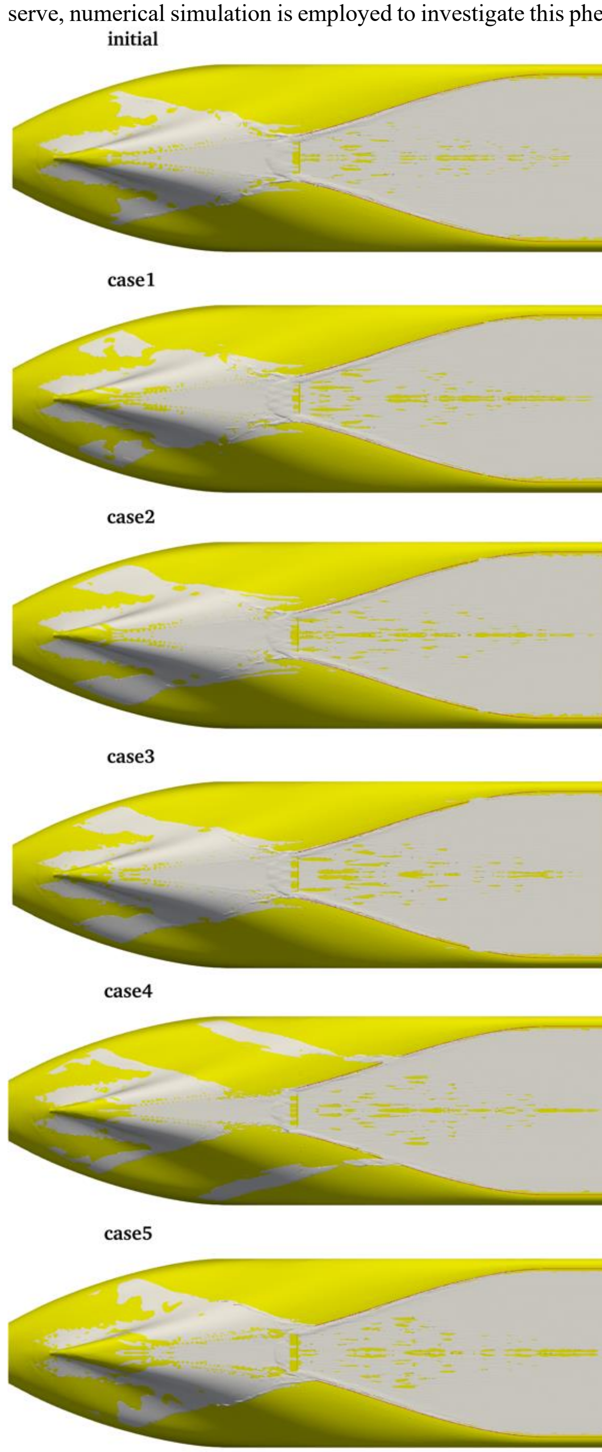

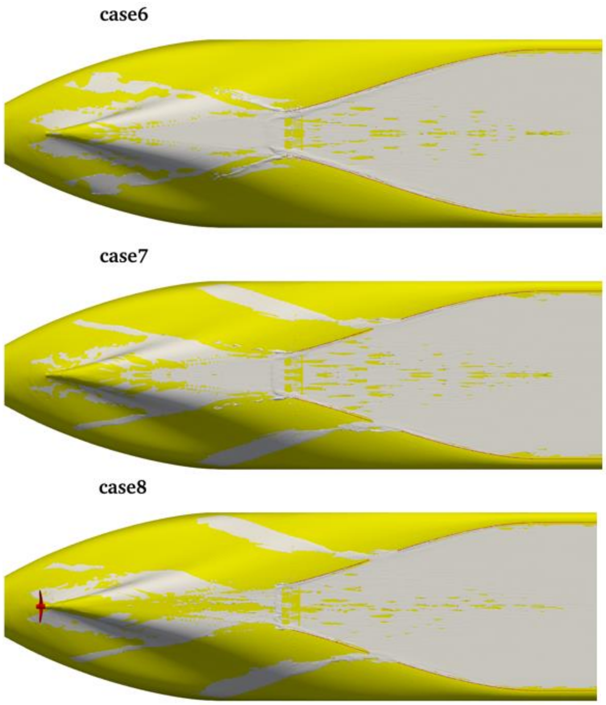

Fig. 10 Instantaneous distribution of the gas layer at the hull bottom (120 s)

Sampling and statistical analysis were conducted on the propeller disk, with the sampling positions specified in Fig. 11. The sampling region on the propeller disk has an inner radius of 0.15 m and an outer radius of 0.88m. Eventually, the instantaneous gas distribution on the propeller disk at 120 s was obtained, as presented in Table 3 and Fig. 12. The gas volume integral value over the impeller disk surface is obtained by integrating the gas volume fraction within each grid over the grid volume.
As can be seen from the table, the original case (with no openings on the bottom baffle) exhibits the highest gas content, while case 8 shows the lowest. The gas contents of case 6 and case 7 are also significantly lower than those of the original model. In terms of gas distribution, Fig. 12 indicates that gas accumulates at the propeller hub, with gas accumulation also occurring directly above the hub. Gas is barely detected in other regions of the propeller disk. It can be concluded that after entering the vicinity of the propeller disk, the gas mainly concentrates at the two aforementioned locations.

Fig. 11 The sample propeller disk position

Table 3 Instantaneous gas content of the propeller disk (120 s)

case	initial	case1	case2	case3	case4
Air content (10^{-3})	0.8648	0.8157	0.77447	0.66393	0.6854
case	case5	case6	case7	case8	
Air content (10^{-3})	0.7065	0.685	0.6757	0.46269	

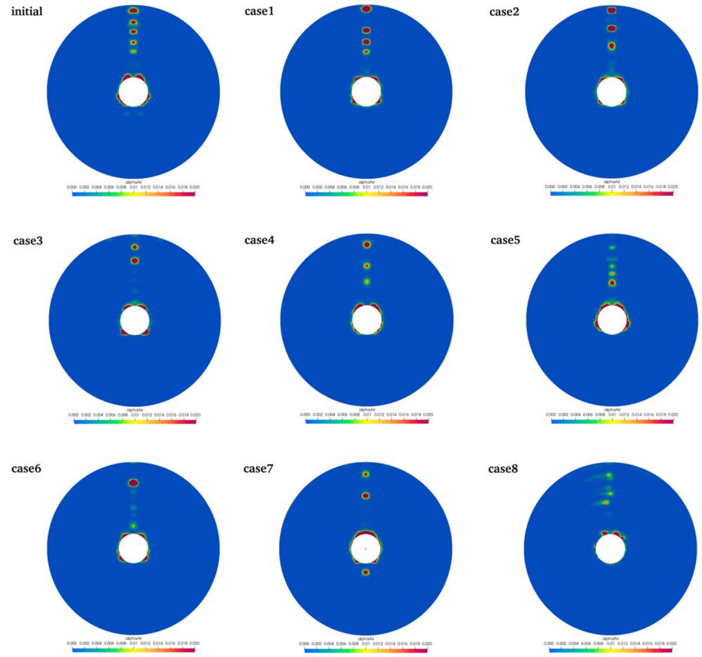

Fig. 12 Instantaneous gas content of the propeller disk (120 s)

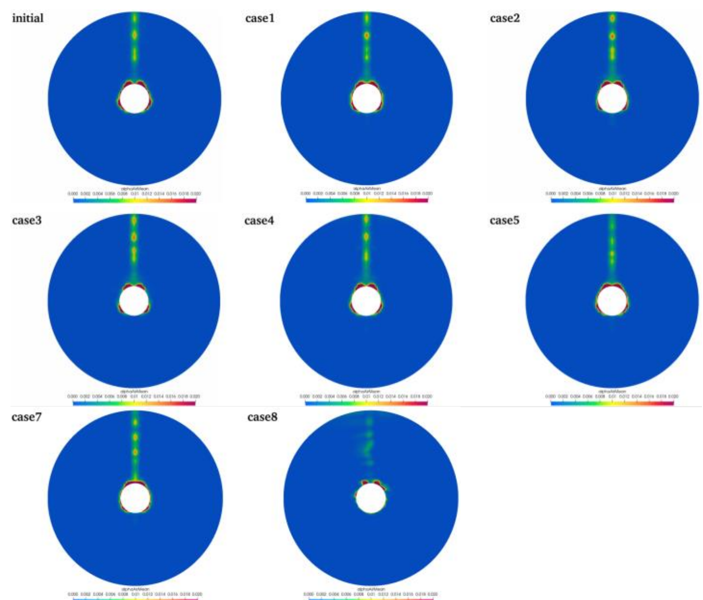

Fig. 13 Average gas content distribution on the propeller disk (120–130 s)

Table 4 Average gas content of the propeller disk (120-130 s)

case	Initial	Case1	Case2	Case3	Case4
Air content (10^{-3})	0.8241	0.7821	0.7665	0.7285	0.79362
case	Case5	Case7	Case8		
Air content (10^{-3})	0.7649	0.7416	0.5119		

Fig. 13 and Table 4 present the average gas content distribution on the propeller disk and the quantitative data of the average gas content on the propeller disk, respectively. First of all, it can be seen from the table that case 8 with the propeller is still the case with the lowest gas content, while the original case has the highest gas content. Among other schemes, cases 7 and 3 also show relatively low gas content. The above

distribution pattern is basically consistent with the instantaneous results. In terms of gas layer distribution, it is also basically consistent with the instantaneous flow field distribution. For case 8 with the propeller, the rotational effect of the gas caused by propeller rotation can be observed. To further investigate cases 7 and 8, explore the influence of the propeller on the average gas content on the propeller disk, and analyze the underlying mechanism, comprehensive visualization and comparison were conducted for the gas layer velocity distribution, streamline distribution, and mesh resolution distribution, as shown in
Fig. 14,
Fig. 15, Fig. 16,
Fig. 17, Fig. 18, and Fig. 19.

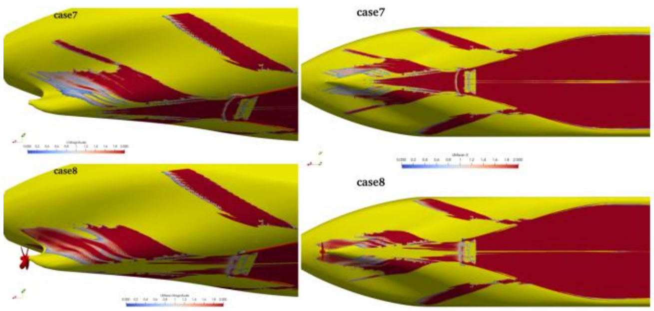

Fig. 14 Velocity of the average gas layer for case 7 and case 8

It can be observed from the gas layer velocity distribution that due to the propeller suction effect, the regional distribution of the gas layer at the hull stern shifts significantly backward, approaching the propeller hub but without covering it, see
Fig. 14. The two cases have the same mesh resolution in the propeller region of the hull, which ensures that there is no numerical dissipation issue caused by inconsistent meshes in this area.

Fig. 15 and Fig. 16 are the streamline distribution at the propeller region for case 7 and case 8. From this figure, it can be observed that the rotation of the propeller exerts an influence on the tail streamlines. Affected by the propeller rotation, both the velocity distribution and the streamline distribution exhibit significant changes, in comparison with case 7, where no propeller is installed.

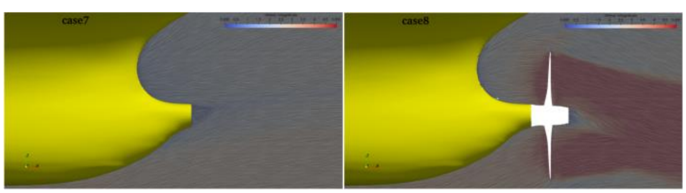

Fig. 15 Streamline distribution at the propeller region for case 7 and case 8

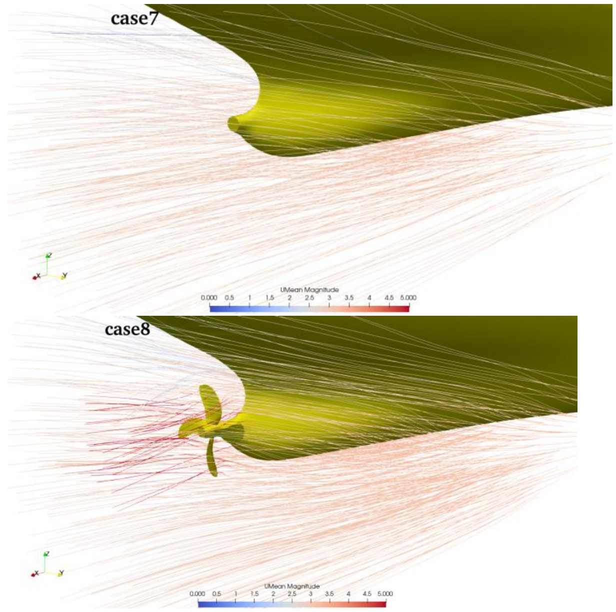

Fig. 16 Streamlines at the propeller for case 7 and case 8

Fig. 18 is the air layer distribution at the mid-longitudinal section of the hull stern for cases 7 and 8. It can be clearly observed from the figure that there exists a discontinuity phenomenon in the gas layer distribution. Specifically, a distinct discontinuity occurs when the gas layer enters the MRF (Multiple Reference Frame) region. This phenomenon may compromise the calculation accuracy of the gas holdup on the impeller disk surface.
To verify whether this phenomenon arises from numerical dissipation caused by grid resolution variation, the grid resolution at the impeller disk surface is presented in Fig. 18 and Fig. 19. As can be seen from the figures, the grid resolution at the propeller position remains consistent between Cases 7 and 8. Therefore, the discontinuity phenomenon of the gas layer is not induced by grid resolution issues.
Instead, this phenomenon is highly likely to be caused by the adopted MRF method. Owing to the limitations of the numerical method, the gas layer generates a discontinuity after entering the rotating MRF region. This phenomenon requires further focused attention and in-depth investigation in subsequent studies, so as to improve the accuracy of numerical calculations of the propeller performance based on the gas holdup at the propeller position.

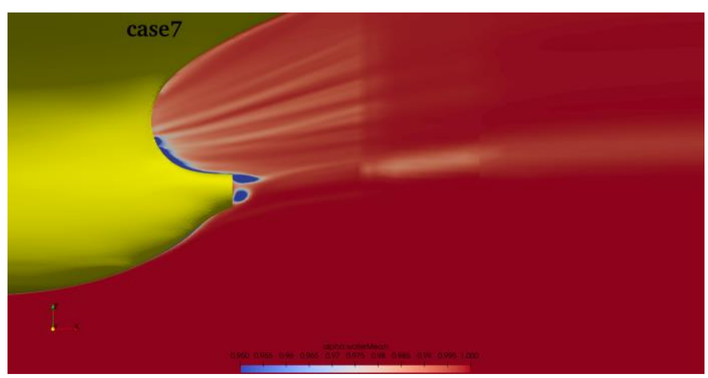

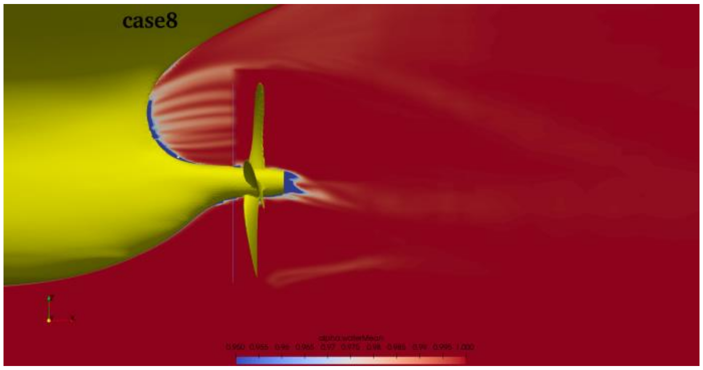

Fig. 17 air layer distribution at the mid-longitudinal section of the hull stern for case 7 and case 8

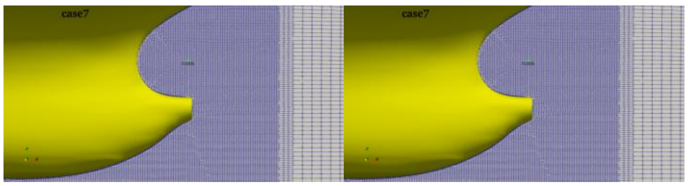

Fig. 18 Mesh comparison at the propeller region for case 7 and case 8

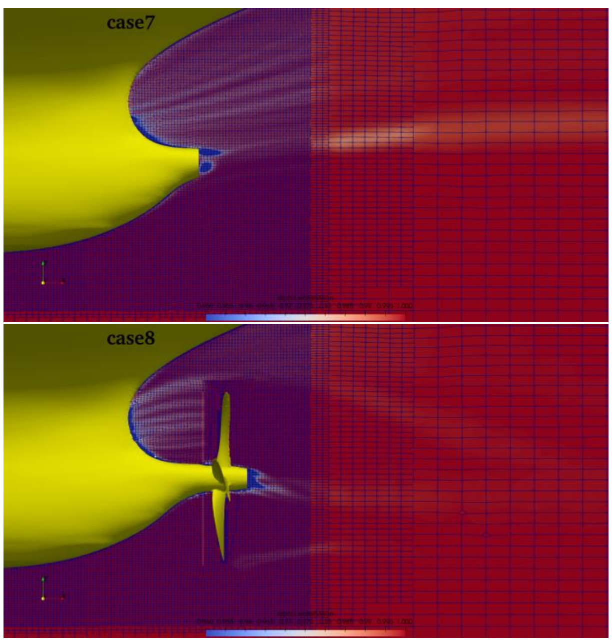

Fig. 19 Mesh resolution at the mid-longitudinal section of the hull stern for case 7 and case 8

As can be seen from the gas distribution at the mid-longitudinal section, compared with the gas distribution in the case without a propeller (case 7), an obvious velocity discontinuity occurs in the MRF region, and discontinuous variations arise in the velocity field inside the entire rotating MRF region. It is speculated that this phenomenon constitutes an important contributing factor to the difference in gas content on the propeller disk between the two cases.

we mainly focus on two aspects: the first is the morphological evolution of the air layer beneath the hull bottom, and the second is the influence of the air layer on the propeller disc plane at the stern. Emphasis is placed on the air void fraction in the propeller disc plane, as well as the air void fraction under actual propeller operating conditions.

Both aspects are worthy of in-depth investigation. At present, only a preliminary macroscopic presentation and discussion are provided in this paper. In future work, we will further conduct an in-depth study on the morphology of the hull air layer and its influence on the performance of the stern propeller.

CONCLUSIONS

Numerical simulations of the gas layer reduction were carried out for full-scale ships with different bottom baffle opening schemes. Meanwhile, the influence of the presence and absence of an actual propeller on the gas layer morphology at the hull bottom was investigated, with a focus on the variation characteristics of the gas content on the propeller disk.

The simulation results indicate that opening holes on the bottom baffle to induce the gas layer to escape toward both sides exerts a certain beneficial effect on reducing the gas content on the propeller disk. However, this beneficial effect cannot be expressed stably and quantitatively, and no obvious regularity is observed in this report. The presence of the propeller may cause the backward shift of the gas layer ascending zone, but the zone will not shift backward to the propeller hub. Through the analysis of the gas content distribution on the propeller disk, it is found that the existing Multiple Reference Frame (MRF) method exerts a significant impact on the statistical results of the gas content at the propeller. When the gas enters the MRF region, an obvious gas layer discontinuity phenomenon occurs. Therefore, further improvement and optimization of the numerical simulation method for cases with a propeller are required in subsequent research to resolve or eliminate this phenomenon.
In this paper, numerical simulation methods are adopted to investigate the air-layer drag reduction at full scale. Due to certain quantitative uncertainties in the computational results at such a scale, the quantitative outcomes of drag reduction are not presented herein. Instead, only the macroscopic flow field of air-layer drag reduction is analyzed and compared. In subsequent research, we will take your advice into account to further analyze the quantitative data and enhance the reliability of the drag calculation results.

The above numerical study conducts a comprehensive preliminary investigation on the gas layer drag reduction of a typical ship from various aspects, and preliminary research conclusions related to the gas layer morphology, gas layer evolution, and gas content on the propeller disk are obtained. Abundant numerical simulation experience has been accumulated in terms of numerical calculation methods and strategies, which lays a solid technical and knowledge foundation for further in-depth research on the gas layer drag reduction characteristics of typical ships in the future.

REFERENCES

An, H., Pan, H., Yang, P., 2022. Research progress of air lubrication drag reduction technology for ships. Fluids 7 (10), 319.

Elbing, B.R., Mäkiharju, S., Wiggins, A., Perlin, M., Dowling, D.R., Ceccio, S.L., 2013. On the scaling of air layer drag reduction. Journal of fluid mechanics 717, 484-513.

Hao, W., Yongpeng, O., Qing, Y., 2019. Experimental study of

air layer drag reduction on a flat plate and bottom hull of a ship with cavity. Ocean Engineering 183, 236-248.
Jagdish, B.N., Xian Brandon, T.Z., Kwee, T.J., Dev, A.K., 2014. Experimental study of air layer sustainability for frictional drag reduction. Journal of Ship Research 58 (01), 30-42.
Mäkiharju, S.A., Perlin, M., Ceccio, S.L., 2012. On the energy economics of air lubrication drag reduction. International Journal of Naval Architecture and Ocean Engineering 4 (4), 412-422.
Mohamad, S.A., Youssef, M., Bennaya, M., Elsherbiny, K., 2025. Experimental and numerical investigation of air layer drag reduction on a flat plate. Alexandria Engineering Journal 121, 436-451.
Wu, H., Ou, Y.-p., 2019. Experimental study of air layer drag reduction with bottom cavity for a bulk carrier ship model. China Ocean Engineering 33 (5), 554-562.
Yanuar, Waskito, K.T., Pratama, S.Y., Candra, B.D., Rahmat, B.A., 2018. Comparison of Microbubble and Air Layer Injection with Porous Media for Drag Reduction on a Self-propelled Barge Ship Model. Journal of Marine Science and Application 17 (2), 165-172.
Zhang, J., Yang, S., Liu, J., 2020. Numerical investigation of frictional drag reduction with an air layer concept on the hull of a ship. Journal of Hydrodynamics 32 (3), 591-604.
Zhao, X., Zong, Z., 2022. Experimental and numerical studies on the air-injection drag reduction of the ship model. Ocean Engineering 251, 111032.